

A crossed-beam experiment for electron impact ionization and dissociation of molecular ions: its application to CO⁺

J Lecointre¹, D S Belic², H Cherkani-Hassani¹, J J Jureta^{1,3} and P Defrance¹

¹ Université catholique de Louvain, Département de Physique, Unité PAMO, Chemin du Cyclotron 2, B-1348 Louvain-la-Neuve, Belgium

² Faculty of Physics, PO Box 386, 11000 Belgrade, Serbia and Montenegro

³ Institute of Physics, PO Box 68, 11081, Belgrade, Serbia and Montenegro

Received 6 January 2006, in final form 18 May 2006

Published 8 August 2006

Online at stacks.iop.org/JPhysB/39/3275

Abstract

A crossed electron–ion beam experimental set-up has been upgraded for the study of electron impact ionization and dissociation of molecular ions by means of ionic product detection. Both the experimental set-up and the data analysis procedures are described in detail for the estimation of (i) absolute cross sections, (ii) kinetic energy release distributions (KERD) and (iii) anisotropies of angular distributions. Absolute cross sections are obtained separately for dissociative excitation (DE) and for dissociative ionization (DI). A double focusing magnetic field analyser is used for the observation of product velocity distributions, in the laboratory frame, at selected electron energies. The KERD in the centre of mass frame is calculated from the measured velocity distribution as well as the anisotropy of the angular distribution with respect to the initial orientation of the molecular ions. Results are reported for dissociative ionization and dissociative excitation of CO⁺ to C⁺ and O⁺ fragments in the energy range from about 5 eV to 2.5 keV. Absolute cross sections for DE at maximum, i.e. for an electron energy around 35 eV, are found to be $(9.69 \pm 2.08) \times 10^{-17} \text{ cm}^2$ and $(6.24 \pm 1.33) \times 10^{-17} \text{ cm}^2$, for C⁺ and O⁺, respectively, and the corresponding threshold energies are found to be $(8.5 \pm 0.5) \text{ eV}$ and $(14.8 \pm 0.5) \text{ eV}$. The DE process leading to C⁺ production is seen to dominate at low electron energies. For DI, the absolute cross section is found to be $(12.56 \pm 2.38) \times 10^{-17} \text{ cm}^2$ around 125 eV and the corresponding threshold energy is $(27.7 \pm 0.5) \text{ eV}$. KERDs, which extend from 0 to 24 eV both for C⁺ and O⁺, exhibit very different shapes at low electron energy but similar ones above 100 eV, confirming the role observed respectively for DE and DI. The groups of states contributing to the different processes are identified by comparing present energies thresholds values and the KERDs with theoretical values. Anisotropies are estimated to be in the range 3–6% for both C⁺ and O⁺.

1. Introduction

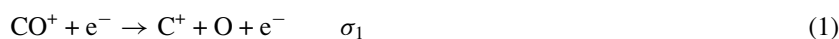
The crossed electron–ion beam configuration is known to be the most efficient method for measurements of absolute ionization cross sections of atomic and molecular ions in a very large energy range, down to a few eV and up to several keV. Since its development (Harrison 1968), the method has been applied to a very large number of atomic, negative and positive ions with charge states as high as +18 for krypton (Khouilid *et al* 2001). Results for polyatomic ions are still rare, the reason being found in the highly dissociative character of small polyatomic ions: when singly charged polyatomic ions are further ionized, the resulting doubly charged ion tends to dissociate rapidly during its flight to the detector. In the experiment, the detection of doubly charged molecular ion allows the characterization of single ionization (SI), whereas the formation of singly charged fragment is due to dissociation which may follow ionization (DI) or even excitation (DE).

Some measurements for polyatomic ions have already been carried out in our laboratory: results on electron impact ionization and dissociation of CO^+ , N_2^+ , O_2^+ , CO_2^+ and H_2^+ have been reported (Belic *et al* 1997, Siari *et al* 1999, Bahati *et al* 2001a, 2001b, Abdellahi *et al* 2004). In the case of dissociation processes, substantial internal energy may be transferred to dissociation fragments, inducing important broadenings of both the angular and the velocity distributions in the laboratory frame, even at large initial ion energy. The angular acceptance of the analysing system, limited by the physical acceptance of the analyser, must be defined large enough to ensure total transmission of the ionic products to the detector. A similar requirement is, in principle, needed for the velocity distribution. However, this condition is not easy to reach and it usually leads to a partial collection of dissociation products. A careful examination and control of this collection allows the determination of the transmission, thanks to magnetic field scans, and subsequently, allows absolute values of the cross section to be determined.

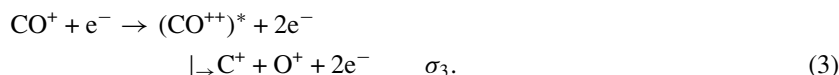
The velocity distributions in the laboratory frame can be deduced from the study of the magnetic scan spectra of product fragments. It was recently (Abdellahi *et al* 2004) demonstrated that kinetic energy release (KER) distributions (KERDs) can be calculated, assuming that distributions of fragment are isotropic with respect to the incident electron velocity. In fact, the anisotropy of angular distributions influences the shape of observed velocity distributions and the magnitude of the associated KERDs. In the present paper, this anisotropy is also calculated and is taken into account in the KERDs estimation.

The present method, which can be used for any molecular ion, is applied to the study of CO^+ . The neutral CO molecule is assumed to be the second most important molecule in the universe after molecular hydrogen (Heubner and Giguere 1980, Störzer *et al* 1995). It is easily ionized and the CO^+ molecular ion is identified as a major constituent in various astrophysical environments, dense interstellar clouds, for instance (Erickson *et al* 1981). It was also seen that this ion could play a role in fusion plasma experiments via dissociative excitation and ionization reactions (Kim *et al* 2000), which are observed close to the plasma border.

Few electron impact experiments have been performed for CO^+ . In our laboratory, cross sections were reported (Belic *et al* 1997) for single ionization (SI, detection of the CO^{++} ions) and for asymmetric dissociative ionization (ADI, dissociation to doubly charged fragments C^{++} and O^{++}). This work indicated that CO^{++} ions are highly unstable against dissociation so that only a small fraction of them survive up to the detector. Dissociative recombination and excitation of CO^+ have been studied in the low energy range (0–50 eV) by Mitchell *et al* (1984) in a merged electron–ion beam experiment (MEIBE1) and by Rosen *et al* (1998) at the CRYRING (CRYogenic RING) storage ring at the Manne Siegbahn Laboratory. None of these experiments could separate the C formation from the O one:



In the present experiment, singly charged C^+ and O^+ ions are detected separately. Each ion may arise from one of the two dissociative excitation (DE) reactions (1) or (2) and also from the dissociative ionization (DI) reaction (3), above the ionization threshold:



CO^+ ionization leads to the formation of doubly charged CO^{++} ions, mostly in excited states (designated by * in equation (3)), which consequently dissociate easily into the ion pair. The measured cross sections, $\sigma_{1,3}$ and $\sigma_{2,3}$, correspond to the mixing of two dissociative reactions ($\sigma_{1,3} = \sigma_1 + \sigma_3$ and $\sigma_{2,3} = \sigma_2 + \sigma_3$) for C^+ and for O^+ , respectively. A specific procedure was developed to estimate σ_1 , σ_2 and σ_3 , separately and is described later in this paper.

In the next section, the experimental set-up is described and the data analysis method is detailed for the estimation of (i) absolute cross sections, (ii) KERDs and (iii) anisotropies. Finally, the experimental procedure is presented. Section 3 is devoted to the description and the discussion of the results obtained for reactions (1), (2) and (3).

2. Apparatus and experimental method

2.1. Experimental set-up

In this experiment, the animated crossed electron–ion beam method is applied (Defrance *et al* 1981). The apparatus has been previously described (Bahati *et al* 2001b) and only the main modifications are presented here. The experimental set-up is schematically shown in figure 1. Ions are extracted from an electron cyclotron resonance (ECR) ion source (1) and accelerated to 8 keV (2). The ion beam is selected by means of a double focusing 90° magnetic analyser (3), additionally focused and purified by a 45° spherical electrostatic deflector (4) and directed into the collision region. Particular attention was devoted to the design of the beam transport from the source to the collision region, in order to avoid possible sources of errors associated with the mass analysis of the primary beam. The ion beam is collimated by a set of apertures into the collision region. The ribbon-shaped electron beam (5) is focused in the collision region where it crosses the ion beam, at right angles.

Product ions are separated from the primary ion beam by means of a double focusing 90° magnetic analyser (6). A set of movable Faraday cups (7) is placed in order to collect the primary ion beam, depending on the initial and final ion mass and charge values. Total collection of primary ions is ensured by the appropriate size of the cups and secondary emission of electrons or ions is prevented by the magnetic field or by suitable suppressing electrodes.

Product ions are deflected along an arc with a fixed radius of curvature of 0.30 m to the detection system. The magnetic analyser was specially designed to transmit ions produced by dissociation processes, with the largest expected KER. The angular acceptance is 0.1 radian, which is large enough to convey to the detector all the ions selected by the variable slit (8) at a fixed ion velocity. The velocity distribution is obtained by scanning the magnetic field. Product ions are further deflected by a 90° electrostatic spherical deflector (9) and directed onto a channeltron detector (10).

A positive voltage up to 2000 V may be applied to the electrodes surrounding the interaction region so that the energy of positive ions formed inside this region is increased.

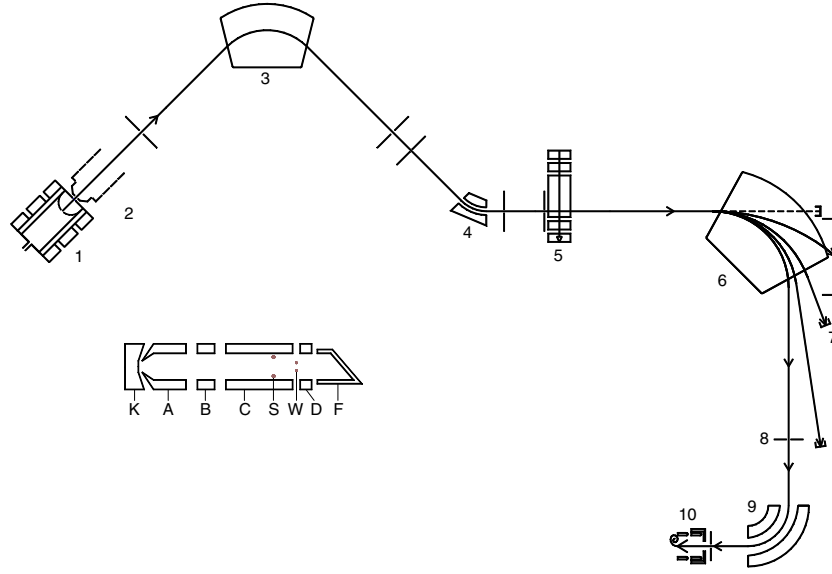


Figure 1. Schematic diagram of the apparatus: (1) ECR ion source, (2) acceleration region, (3) magnetic mass selector, (4) spherical electrostatic deflector, (5) electron gun, (6) magnetic analyser, (7) Faraday cups, (8) variable slit, (9) spherical electrostatic deflector, (10) detector. The inset shows a schematic plan of the electron gun: (K) cathode, (A) anode, (B) focusing and deflecting electrodes, (C) collision region, (S) wires for the sweeping speed measurement, (W) wires, (D) suppressors, (F) Faraday cup.

Ions created outside this region do not undergo this kinetic energy displacement and may be rejected by the magnetic analyser.

The electron gun is schematically shown in the inset of figure 1. A ribbon-shaped electron beam is extracted from a Pierce-type cathode (K) anode (A) configuration. The pair of plates (B) acts simultaneously as a lens and as the beam deflector for the application of the animated crossed beams method. The electron beam crosses the ion beam inside the electrodes (C). During the measurements, the electron beam is swept across the ion beam, in a linear see-saw motion at a constant speed u , which is measured by means of two thin wires (S) located on both sides of the ion beam symmetrically, perpendicular to the electron beam trajectory. The electrons are collected in a Faraday cup (F). Suppression plates (D) provide total beam collection and prevent secondary electrons from interacting with the ion beam. A voltage can be applied to wires (W) in order to establish a potential barrier or a potential well to check the influence of residual ions trapped in the electron beam. All the electrodes are made of ARCAP amagnetic alloy. Magnetic shielding located inside the vacuum chamber keeps the residual magnetic field below 2×10^{-7} T.

2.2. Cross-section measurements

In collision experiments, the cross section (σ) is proportional to the count rate (N), the proportionality factor being the luminosity (L):

$$N = L\sigma. \quad (4)$$

In experiments where the particle beams interact under an angle Θ , the luminosity is related to the form-factor F (Defrance *et al* 1981) by

$$L = \frac{AI_e I_i}{F} \quad (5)$$

where I_e and I_i are the electron and ion beam current intensities, respectively, and F is the effective height over which the beams interact. The kinematic factor (A) is given by

$$A = \frac{(v_e^2 + v_i^2 - 2v_e v_i \cos \Theta)^{1/2}}{v_e v_i q e^2 \sin \Theta}. \quad (6)$$

In this expression e and qe , v_e and v_i , are the charges and velocities of electrons and ions, respectively. The international unit system is used through this section.

In the animated beam method (Defrance *et al* 1981), the electron beam is swept across the ion beam in a linear see-saw motion at a constant speed u , implying that the measurement of the beam density profiles is not required anymore. The amplitude of the movement is large enough so that the beams do not overlap any longer in the extreme positions. The total number of events K produced during one complete electron beam movement is related to the cross section by the following expression:

$$\sigma = \frac{uK}{AI_e I_i \gamma} \quad (7)$$

where γ is the detector efficiency. The animated and the static beam methods are connected by the relation $uK = NF$.

In the real experiment, the total displacement is divided into n steps for the data recording purpose, so that the practical form of (7) for the cross section evaluation includes

$$K = \sum_{j=1}^n \frac{k_j \left(\frac{u_j}{u} \right)}{\left(\frac{I_{ej}}{I_e} \right) \left(\frac{I_{ij}}{I_i} \right)} \quad (8)$$

where k_j , u_j , I_{ej} and I_{ij} are the ion signal, sweeping velocity, the electron and ion currents at the j th step, respectively, and u , I_e and I_i are the corresponding average values of electron beam sweeping speed, electron and ion currents. This expression takes into account irregularities of the sweeping speed and fluctuations of the beam intensities under the one and only hypothesis that beam density profiles do not vary even when current intensities fluctuate during the movement.

The relative velocity v_r between electrons and ions is given by

$$v_r = (v_e^2 + v_i^2 - 2v_e v_i \cos \Theta)^{1/2}. \quad (9)$$

The true interaction energy E_e (eV) is obtained from (9). For beams interacting at right angles and assuming $m_i \gg m_e$, it is given by

$$E_e = V_e + \frac{m_e}{m_i} (qV_i - V_e) \quad (10)$$

where V_e and V_i , m_e and m_i are the acceleration voltages and masses of electrons and ions, respectively. In the current experiment, the electron energy is corrected for a contact potential difference (ΔV) which is usually determined by measuring accurately the appearance potential of a well-known physical process. Depending on the potential applied to the interaction region, ΔV is held between 1 and 5 eV. According to previous experiments, the electron energy spread (full width at half maximum, FWHM) is estimated to be less than 1 eV.

The sweeping speed is determined by measuring the time difference t between successive crossings of the electron beam with the wires (S), which are distant from each other by 7.9 mm. The electron and ion currents collected in the Faraday cups are frequency converted and recorded in two separate counters during the measurement. The frequency of the sweeping voltage is about 385 Hz and the duration of the measurement may vary from 1 min to about 1 h.

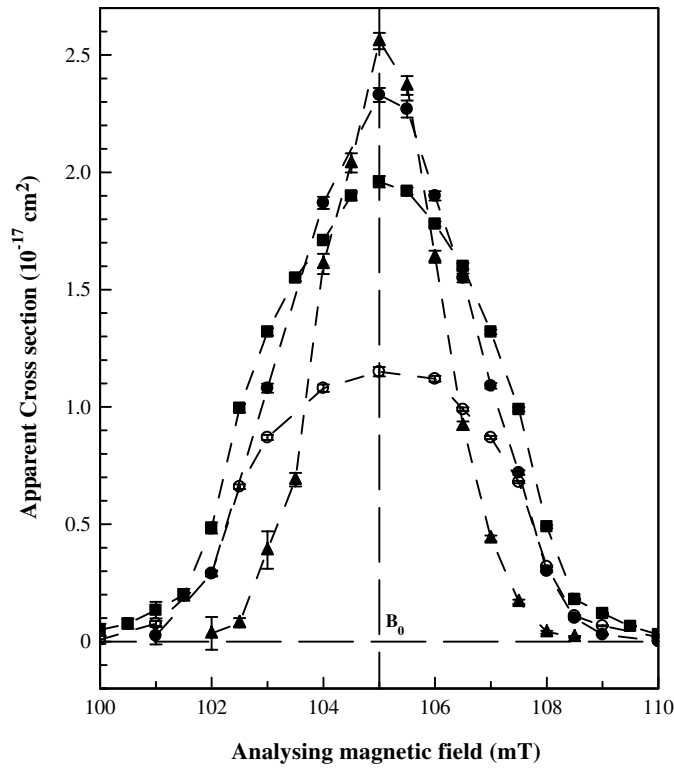


Figure 2. Apparent cross sections for C^+ production versus magnetic field for electron energies: 17.1 eV (\blacktriangle), 45.1 eV (\bullet), 145.1 eV (\blacksquare) and 495.1 eV (\circ).

The ion detector signal is counted and stored in a multichannel analyser in the multiscaling mode, synchronously with the electron beam sweeping voltage. The pressure is kept below 1×10^{-9} mbar in the collision chamber during the measurement, in order to reduce the noise. In the case of CO^+ , the energy of the ion beam (8 keV) is high enough to ensure the 100% efficiency of the channeltron detector.

2.3. Kinetic energy release distributions

Due to the transfer of internal energy, dissociation fragments exhibit both the broad velocity and angular distributions in the laboratory frame. The product transmission being not total (Abdellahi *et al* 2004), the apparent cross section $\sigma_m(B)$ is measured as a function of the analyser magnetic field B in order to determine the cross-section differential with respect to the magnetic field ($d\sigma(B)/dB$) (see section 2.5).

On the one hand, the product ion velocity in the laboratory frame v is related to the analyser magnetic field B ($v = qRB/m$) and, consequently, the velocity distribution ($d\sigma(v)/dv$) is

$$\frac{d\sigma(v)}{dv} = \frac{m}{qR} \frac{d\sigma(B)}{dB}. \quad (11)$$

Here, m is the fragment ion mass and R is the radius of its trajectory in the analyser magnetic field. Examples of cross-section measurements as a function of the magnetic field $\sigma_m(B)$ are shown in figures 2 and 3 for the case of C^+ and O^+ , respectively.

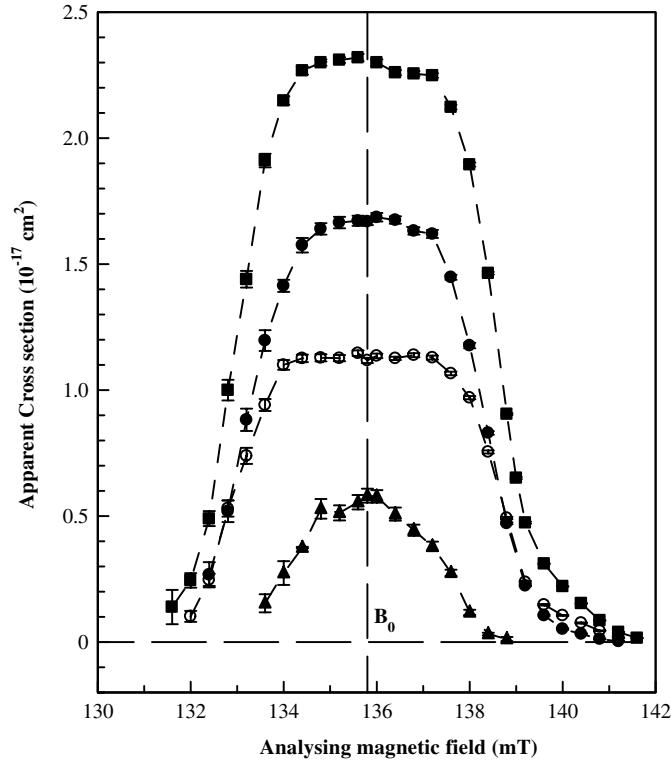


Figure 3. Apparent cross sections for O^+ production versus magnetic field for electron energies: 17.1 eV (\blacktriangle), 45.1 eV (\bullet), 145.1 eV (\blacksquare) and 495.1 eV (\circ).

On the other hand, the differential cross section $d\sigma(v)/dv$ can be expressed as a function of the cross section in the centre of mass frame:

$$\frac{d\sigma(v)}{dv} = \int_0^{\theta_{LM}(v)} \int_0^{2\pi} \frac{1}{w^2} \frac{d^3\sigma(w, \theta, \phi)}{dw d\Omega} v^2 \sin \theta_L d\theta_L d\phi. \quad (12)$$

In this expression, $\frac{d^3\sigma(w, \theta, \phi)}{dw d\Omega}$ represents the differential cross section for the ejection of the considered fragment in the centre of mass, with speed w , and within a solid angle $d\Omega$ around the direction defined by the emission angles θ and ϕ . θ is defined with respect to the velocity of the centre of mass v_c and ϕ is the azimuthal angle. In the laboratory frame, the ejection angle θ_L is also defined with respect to v_c . In this configuration, w is given by

$$w^2 = v^2 + v_c^2 - 2vv_c \cos \theta_L. \quad (13)$$

For a fixed v , each θ_L angle corresponds to one speed w . In particular, the upper limit $\theta_{LM}(v)$ corresponds to the ejection of the most energetic fragment ($w = w_M$) and the lower limit ($\theta_L = 0$) corresponds to the less energetic fragment ($w = w_m = |v - v_c|$). At the first order, the maximum ejection angle is reached for $v = v_c$ and $w = w_M$, so that the angular acceptance of the analysing system must be defined large enough to ensure the total transmission of ionic products within a cone of angle $\theta_{LM}(v_c)$. It is worth mentioning that ions emitted in the laboratory frame in the forward ($v > v_c$) or in the backward ($v < v_c$) direction correspond to ejection angles $0 < \theta < \pi/2$ or $\pi/2 < \theta < \pi$, respectively. Taking into account the fact that v is constant over the surface of integration, the differentiation of (13) allows θ_L to be replaced

by w in (12). The derivative of equation (12) with respect to v , taking into account expression (13) and integrating over ϕ leads to the velocity distribution of fragments ejected along the centre of mass velocity ($\theta = \phi = 0$):

$$\frac{d^3\sigma(w_m, 0, 0)}{dw d\Omega} = \frac{v_c(v_c - v)}{2\pi} \frac{d}{dv} \left(\frac{1}{v} \frac{d\sigma(v)}{dv} \right). \quad (14)$$

The total kinetic energy released (KER_m) to dissociation fragments emitted along the centre of mass velocity is given by

$$\text{KER}_m = \frac{m^2 w_m^2}{2\mu}. \quad (15)$$

In this formula, μ is the reduced mass of the fragments. Finally, the KERD along the centre of mass velocity is expressed as

$$\frac{d^3\sigma(\text{KER}_m, 0, 0)}{d\text{KER} d\Omega} = \frac{1}{2\pi} \frac{\mu}{m^2} \frac{v_c(v_c - v)}{w_m} \frac{d}{dv} \left(\frac{1}{v} \frac{d\sigma(v)}{dv} \right). \quad (16)$$

2.4. Angular distributions

Integration of expressions (14) or (16) over w_m or KER, respectively, allows $\frac{d^2\sigma(0,0)}{d\Omega}$ to be computed:

$$\frac{d^2\sigma(0, 0)}{d\Omega} = \int_0^\infty \frac{v_c(v_c - v)}{w_m} \frac{d}{dv} \left(\frac{1}{v} \frac{d\sigma(v)}{dv} \right) dw_m \quad (17a)$$

or

$$\frac{d^2\sigma(0, 0)}{d\Omega} = \int_0^\infty \frac{1}{2\pi} \frac{\mu}{m^2} \frac{v_c(v_c - v)}{w_m} \frac{d}{dv} \left(\frac{1}{v} \frac{d\sigma(v)}{dv} \right) d\text{KER}. \quad (17b)$$

It is readily demonstrated that these expressions are related to the measured quantities in the following manner:

$$\frac{d^2\sigma(0, 0)}{d\Omega} = \frac{v_c}{2\pi} \int_{v_c}^{v_M} \frac{1}{v} \frac{d\sigma(v)}{dv} dv. \quad (18)$$

The angular distribution of dissociation products depends on the orientation of the molecule at the moment where dissociation takes place. Assuming a uniform angular distribution of the molecular axis in the primary beam and if the rotation period is longer than the dissociation time, the angular dissociation pattern then directly reflects the dependence of the cross section upon the initial orientation angles. Following Busalla *et al* (1999), the product angular distribution for a given dissociative process can be described by

$$\frac{d^2\sigma(\alpha, \beta)}{d\Omega} = \frac{\sigma}{4\pi} (1 + \delta P_1(\cos \beta) + \varepsilon P_2(\cos \beta)) \quad (19)$$

where β is the angle between the molecular axis and the incident electron velocity (v_e), α is the azimuthal angle, $P_i(\cos \beta)$ is the Legendre polynomial of i th order. According to the cylindrical symmetry around the electron beam axis, the distribution given by (19) does not depend on α . δ and ε are the steric factors: δ reflects the asymmetry of the molecule and ε describes the anisotropy of the distribution with respect to the velocity of the incident electron. The angular distribution (19) is evaluated according to the conditions of the present experiment ($\alpha = 0$ and $\beta = \pi/2$, corresponding to $\theta = 0$ and $\phi = 0$) so that ε can be expressed by means of (18) in terms of the measured cross sections:

$$\varepsilon = 2 \left(1 - \frac{2v_c}{\sigma} \int_{v_c}^{v_M} \frac{1}{v} \frac{d\sigma(v)}{dv} dv \right). \quad (20)$$

Due to the symmetry of interacting beams and the integration procedure, δ cannot be evaluated here.

Expression (19) may be written in different manners, which describes the anisotropy of the dissociation process. Zare *et al* (1967) calculated the differential cross section for the ejection of a proton produced by H_2^+ molecule oriented with respect to the electron beam:

$$\frac{d^2\sigma(\alpha, \beta)}{d\Omega} \approx \cos^2 \chi \cos^2 \beta + \frac{1}{2} \sin^2 \chi \sin^2 \beta. \quad (21)$$

Here, χ defines the direction of the final electron momentum transfer with respect to the initial one. A similar formula was proposed by analogy with results of laser-molecule experiments (Bodeldijk *et al* 1994, 1996):

$$\frac{d^2\sigma(\alpha, \beta)}{d\Omega} = \frac{\sigma_{\parallel} \cos^2 \beta + \sigma_{\perp} \sin^2 \beta}{4\pi}. \quad (22)$$

In this expression, σ_{\parallel} and σ_{\perp} correspond to the angular differential cross sections for dissociation when the molecular axis is parallel and perpendicular to the incident electron beam, respectively. Integration of (22) over the full angular range leads to the total cross section σ in the form

$$\sigma = \frac{\sigma_{\parallel}}{3} + \frac{2\sigma_{\perp}}{3}. \quad (23)$$

For homonuclear molecules, $\delta = 0$ and ε is related to the cross sections in the following way:

$$\varepsilon = \frac{2}{3} \left(\frac{\sigma_{\parallel}}{\sigma} - \frac{\sigma_{\perp}}{\sigma} \right). \quad (24)$$

The present description of differential cross sections implies that the differential cross section $\frac{d^3\sigma(w, \theta, \phi)}{dw d\Omega}$ is separable with respect to the KER and to the angles and may be, on the one hand, evaluated in the conditions of the experiment and, on the other hand, integrated over the full angular range. The comparison of these two results together with (16) allows the full KERD to be expressed in terms of the experimental results:

$$\frac{d\sigma(\text{KER})}{d\text{KER}} = \frac{-2\mu v_c}{m^2(1 - \varepsilon/2)} \frac{d}{dv} \left(\frac{1}{v} \frac{d\sigma(v)}{dv} \right). \quad (25)$$

2.5. Experimental procedure

The full transmission of product fragment ions is achieved in a given angular range but, because of the limited size of the slits, it is usually not available for the broad velocity distribution. As a consequence, only a fraction of the signal is detected for a fixed magnetic field and measured cross sections are not absolute. To overcome this problem and obtain the total signal, different methods are developed. For instance, the detector may be moved mechanically through the velocity distribution (Djuric *et al* 1997). In the present experiment, the velocity distribution is scanned by varying the analysing magnetic field in front of the fixed detector. The total cross section σ is given by

$$\sigma = \int_{-\infty}^{+\infty} f(B) dB \quad (26)$$

with

$$f(B) = \frac{d\sigma(B)}{dB}. \quad (27)$$

The apparent cross section $\sigma_m(B_i)$ is measured at different values of the magnetic field B_i as to cover the whole distribution. At the given field B_i , the apparent cross section is

$$\sigma_m(B_i) = \int_{B_i - \Delta B/2}^{B_i + \Delta B/2} f(B) dB, \quad (28)$$

ΔB corresponds to the acceptance defined by the analysing slit of the magnet. The first derivative of expression (28) with respect to B and the rearrangement of the result leads to

$$f(B) = \frac{1}{1 + \Delta B/2B} f(B - \Delta B/2) + \frac{1 - \Delta B/2B}{1 + \Delta B/2B} f(B - \Delta B). \quad (29)$$

This expression allows the determination of $f(B)$ by computing the derivative of the experimental result $\sigma_m(B_i)$ and finally the total cross section is computed by (26). The repetition of this procedure at each electron energy results in a very long and tedious task.

To avoid this situation, an alternative procedure was introduced to accurately cover the whole energy range without measuring all the distributions. In the first step, the apparent cross section $\sigma_m(E_e)$ is measured versus the electron energy at the central magnetic field B_0 . Working at this field is necessary in order to include the contributions of all the ejection speeds in the centre of mass frame. The second step consists in measuring the distributions for several fixed electron energies E_e (figures 2 and 3) so that absolute cross sections are computed at these energies by means of (26).

The transmission factor η is defined as the ratio of the cross section measured at a fixed analyser magnetic field B_i and the total cross section σ , it can be computed at the selected energies:

$$\eta = \frac{\sigma_m(B_i)}{\sigma} = \frac{\int_{B_i - \Delta B/2}^{B_i + \Delta B/2} f(B) dB}{\int_{-\infty}^{+\infty} f(B) dB}. \quad (30)$$

The transmission factor is estimated over the whole energy range by interpolation and extrapolation of these results. Finally, the apparent cross sections are corrected to obtain the absolute cross sections ($\sigma_{1,3}$ or $\sigma_{2,3}$, for C^+ and O^+ , respectively):

$$\sigma(E_e) = \frac{\sigma_m(E_e)}{\eta(E_e)}. \quad (31)$$

2.6. Separation of DE and DI

Products of reactions (1)–(3) for C^+ and (2)–(3) for O^+ form two velocity distributions whose shapes depend on the various involved KERs (figures 2 and 3). The spectra consist of two main contributions (Bahati *et al* 2001): the upper part (the narrow one) of the distribution corresponds to DE (reactions (1) and (2), low KER) and that the lower part (the wider one) is attributed to DI (reaction (3), large KER due to Coulomb repulsion). A careful examination of the spectra shows the changes of slope which indicate the presence of these two distinct contributions.

The following procedure was developed to separate the individual contributions of the two identified processes. First, the DI signal is isolated by fitting the outer part of the spectrum. Then, the apparent cross section versus the electron energy $\sigma_m^{DI}(E_e)$ is measured for a specific fixed magnetic field, high enough to avoid the DE contribution so that the pure DI contribution is obtained. For example, in the case of the O^+ production, the $\sigma_m(B)$ distribution for $E_e = 22$ eV is narrow (only DE contributes) and vanishes for $B = 138.8$ mT (figure 3). As a consequence, to avoid the DE contribution, the magnetic field is fixed at 140 mT to perform

Table 1. Typical working conditions and estimated uncertainties (1 standard deviation).

Parameter	Typical value	Systematic error (%)	Statistical error (%)
Kinematic factor, A (s mC^{-2})	6.4×10^{-29}	0.5	–
Sweeping speed, u (m s^{-1})	3.75	1.0	1.0
Ion current, I_i (nA)	30	0.5	1.0
Electron current, I_e (mA)	1–3	0.5	1.0
Detection efficiency, γ	1	1	–
Single ionization (CO^{++})			
Counts (K)/luminosity (L) ($10^{20} \text{ Hz cm}^{-2}$)	1.3/3	–	0.8
Cross section, σ_{max} (10^{-17} cm^2)	1.45	1.7	1.9
Dissociation (C^+)			
Counts (K)/luminosity (L) ($10^{20} \text{ Hz cm}^{-2}$)	0.5/1	–	1.5
Transmission factor, η (%)	15	–	5
Cross section, σ_{max} (10^{-17} cm^2)	14.57	1.7	5.5
Dissociation (O^+)			
Counts (K)/luminosity (L) ($10^{20} \text{ Hz cm}^{-2}$)	1.5/3	–	0.5
Transmission factor, η (%)	16	–	5
Cross section, σ_{max} (10^{-17} cm^2)	14.59	1.7	5.3
Dissociative ionization ($\text{C}^+ + \text{O}^+$)			
Counts (K)/luminosity (L) ($10^{20} \text{ Hz cm}^{-2}$)	0.1/2	–	0.7
Transmission factor, η (%)	6	–	11.2
Cross section, σ_{max} (10^{-17} cm^2)	12.56	1.7	11.4

the $\sigma_{\text{m}}^{\text{DI}}(E_e)$ measurements. The transmission $\eta_{\text{DI}}(E_e)$ is calculated at this high magnetic field to put the apparent cross section on an absolute scale by means of the following expression:

$$\sigma_3(E_e) = \frac{\sigma_{\text{m}}^{\text{DI}}(E_e)}{\eta_{\text{DI}}(E_e)}. \quad (32)$$

Absolute values of DE cross sections (σ_1 or σ_2 , for C^+ and O^+ respectively) are obtained by subtracting the DI contribution (σ_3) from the total absolute cross section ($\sigma_{1,3}$ or $\sigma_{2,3}$, for C^+ and O^+ respectively).

3. Results and discussion

Previous results on electron impact SI of CO^+ and on asymmetric dissociative ionization (ADI) to C^{++} and O^{++} fragments have been published (Belic *et al* 1997). As a test, SI cross sections have been measured again, and results were found in very good agreement with the previous data. Present measurements deal with absolute total cross sections for the production of C^+ ($\sigma_{1,3}$) and O^+ ($\sigma_{2,3}$). The subsequent analysis of the experimental results provides us with individual contributions for DE and DI (σ_1 , σ_2 and σ_3 for processes (1), (2) and (3), respectively), KERDs and anisotropies.

3.1. Absolute cross sections for total C^+ and O^+ fragment production

Typical working conditions, statistical and systematic uncertainties of experimental parameters are listed in table 1 (1 standard deviation). The uncertainty associated with the transmission factor is estimated to be 5%. The total uncertainty (90% confidence limit) obtained as the quadratic sum of the statistical and systematic uncertainties at the cross section maximum is found to be 4.2%, 9.5%, 9.2% for σ_{SI} , $\sigma_{1,3}$ and $\sigma_{2,3}$, respectively. Moreover, the uncertainty

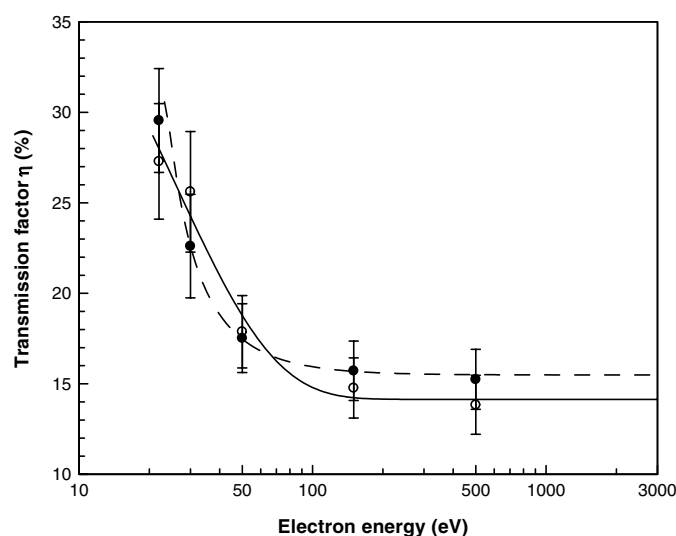


Figure 4. Transmission factors and fitting curves for C^+ ((○) and (—)) and for O^+ ((●) and (---)).

associated with the fitting procedure is estimated to be 10% so that the total uncertainty for σ_3 (90% confidence limit) is estimated to be 18.9%, and consequently total uncertainties for σ_1 and σ_2 are found to be 21.2% and 21.0% respectively. Absolute cross sections ($\sigma_{1,3}$, $\sigma_{2,3}$, σ_1 , σ_2 and σ_3) are listed in table 2, together with the associated total uncertainties (90% confidence limit).

Magnetic scans were performed at electron energies of 17.1, 25.1, 45.1, 145.1 and 495.1 eV (figures 2 and 3, for C^+ and O^+ , respectively; for clarity reasons, 25.1 eV distributions are not shown). Generally, the spectra exhibit a maximum around the central field B_0 (105 mT and 135.8 mT for C^+ and O^+ , respectively) which corresponds to fragments emitted with $v = v_c$. At low energy (17.1 eV), the distribution is narrow (low KER), the spectra represent DE only. For electron energies above the DI threshold, the width increases due to the large KER associated with DI. At 495.1 eV both spectra are very wide and they seem to represent the DI contribution only. They have almost the same magnitude, what is expected, since C^+ and O^+ fragments originate from the same DI reaction.

Transmission factors are determined directly from each measured distribution (equation (31)) and results are shown in figure 4 together with the corresponding fitting curves. They range from 30%, at low energies, to about 15%, at high energies. The transmission factor is directly linked to the width of the velocity distribution: close to the threshold, it tends towards the maximum; for high energies, it is lowered since the velocity distribution becomes wider and above 100 eV, it is seen to reach a constant value.

In the low energy range (below the ionization threshold, 25.1 eV), $\sigma_{1,3}$ and $\sigma_{2,3}$ are equal to σ_1 and σ_2 , respectively, only DE contributes to the signal. The pronounced shoulder observed at about 25 eV for $\sigma_{1,3}$ is due to the opening of the DI channel. Above 100 eV, $\sigma_{1,3}$ and $\sigma_{2,3}$ are seen to be nearly equal and DI is found to be the dominant contribution (figure 5). Table 3 lists present observed threshold energies together with other experimental results for processes (1), (2) and (3). Calculated thresholds and KER are also reported for the involved dissociative states. The KER ranges are estimated as the limits determined on the potential curves at the nuclear distances corresponding to the Franck–Condon turning points for the ground state CO^+ . Experimental KER ranges are deduced from the analysis of observed KERDs.

Table 2. Absolute cross sections for total C⁺ and O⁺ production and for DE and DI (10⁻¹⁷ cm²).

E_e (eV)	Total $\sigma_{1,3}$: C ⁺		Total $\sigma_{2,3}$: O ⁺		DE σ_1 : C ⁺		DE σ_2 : O ⁺		DI σ_3 : C ⁺ + O ⁺	
	σ	$\Delta\sigma$	σ	$\Delta\sigma$	σ	$\Delta\sigma$	σ	$\Delta\sigma$	σ	$\Delta\sigma$
5.1	0	0.14			0	0.14				
6.1	0.04	0.12			0.04	0.12				
7.1	0.40	0.20			0.4	0.21				
8.1	0.63	0.18	0.00	0.13	0.63	0.21	0.003	0.13		
9.1	1.59	0.26	0.04	0.03	1.59	0.40	0.039	0.03		
10.1			0.04	0.03			0.04	0.03		
11.1	3.46	0.43	0.04	0.03	3.46	0.79	0.04	0.03		
12.1			0.12	0.03			0.12	0.04		
13.1	6.03	0.65	0.22	0.04	6.03	1.32	0.22	0.06		
15.1	7.01	0.70	0.58	0.07	7.01	1.50	0.58	0.13		
17.1			1.24	0.13			1.24	0.27		
18.1	7.91	0.78			7.91	1.69				
19.1			2.08	0.21			2.08	0.44		
21.1	8.26	0.83	3.08	0.30	8.26	1.77	3.08	0.65		
23.1									-0.008	0.18
25.1	8.99	0.88	4.47	0.43	8.90	1.90	4.38	0.93	0.091	0.02
27.1	9.40	0.91			9.28	1.98			0.12	0.10
29.1									0.38	0.15
30.1	9.89	0.98	5.71	0.53						
31.1									0.55	0.18
33.1									0.88	0.20
35.1	10.75	1.03	7.04	0.66	9.69	2.08	5.98	1.28	1.06	0.24
37.1									1.42	0.32
40.1	11.54	1.14	8.24	0.77	9.54	2.07	6.24	1.33	2.00	0.40
45.1	12.08	1.21	9.26	0.86	8.95	1.98	6.13	1.32	3.13	0.62
50.1	12.42	1.20								
55.1	12.68	1.28	10.74	0.99	7.33	1.68	5.39	1.18	5.35	1.03
65.1	12.95	1.27	11.48	1.06	6.13	1.41	4.66	1.04	6.82	1.31
70.1	13.16	1.28								
75.1	13.52	1.32	12.09	1.12	5.07	1.18	3.64	0.83	8.45	1.61
80.1	13.54	1.34								
85.1	13.85	1.34	12.82	1.19	4.33	1.03	3.3	0.79	9.52	1.81
90.1	13.77	1.33								
95.1	14.23	1.40	13.96	1.29	3.46	0.90	3.19	0.73	10.77	2.04
105.1			14.27	1.33			2.8	0.70	11.47	2.18
115.1	14.57	1.40	14.54	1.34	2.39	0.62	2.36	0.53	12.18	2.31
125.1	14.20	1.36	14.51	1.34	1.64	0.49	1.95	0.50	12.56	2.38
135.1	13.99	1.34	14.59	1.35	1.55	0.44	2.15	0.51	12.44	2.35
145.1	13.63	1.31	14.33	1.32	1.42	0.43	2.12	0.51	12.21	2.31
155.1			13.96	1.29			1.98	0.49	11.98	2.27
165.1	13.25	1.30								
175.1			12.68	1.17			1.31	0.35	11.37	2.15
195.1	12.22	1.17	12.14	1.12	1.58	0.47	1.5	0.41	10.64	2.02
245.1	10.81	1.05	10.50	0.97	1.61	0.51	1.3	0.38	9.20	1.75
295.1	9.94	1.02	9.69	0.90	1.46	0.61	1.21	0.34	8.48	1.61
345.1	9.40	0.95								
395.1	8.84	0.90	8.49	0.79	1.63	0.58	1.28	0.34	7.21	1.37
495.1	7.62	0.75	7.66	0.71	1.54	0.46	1.58	0.39	6.08	1.16
595.1	6.75	0.67	6.82	0.63	1.43	0.42	1.5	0.37	5.32	1.01
695.1	6.24	0.64								

Table 2. (Continued.)

E_e (eV)	Total $\sigma_{1,3}$: C ⁺		Total $\sigma_{2,3}$: O ⁺		DE σ_1 : C ⁺		DE σ_2 : O ⁺		DI σ_3 : C ⁺ + O ⁺	
	σ	$\Delta\sigma$	σ	$\Delta\sigma$	σ	$\Delta\sigma$	σ	$\Delta\sigma$	σ	$\Delta\sigma$
795.1	5.73	0.62	5.65	0.52	1.31	0.48	1.23	0.31	4.42	0.84
895.1	5.14	0.52								
995.1	4.92	0.49	4.90	0.46	1.18	0.34	1.16	0.29	3.74	0.71
1195.1	4.34	0.47								
1495.1	3.54	0.38	3.71	0.34	0.81	0.30	0.98	0.24	2.73	0.52
1995.1	2.89	0.29	3.09	0.29	0.59	0.21	0.79	0.20	2.30	0.44
2195.1	2.74	0.29								
2495.1	2.52	0.29	2.72	0.26	0.58	0.25	0.78	0.19	1.94	0.37

3.2. Dissociative ionization cross sections

The individual detection of each product (C⁺ and O⁺) of the DI reaction (3) provides us with two independent estimations of σ_3 . Measurements of $\sigma_m^{\text{DI}}(E_e)$ were performed at magnetic fields of 108.5 mT and 140 mT for C⁺ and O⁺, respectively, where only the DI contribution is present. As a result, the two sets of absolute cross sections (σ_3) were found to agree with each other within $\pm 10\%$ in the whole energy range. Only results for O⁺ fragments are kept for discussion, since the experiment led to much lower statistical uncertainties in this case. The cross section maximum is found to be $(12.56 \pm 2.38) \times 10^{-17} \text{ cm}^2$ at the electron energy of 125.1 eV. This value is almost an order of magnitude higher than the value obtained for simple ionization (Siari *et al* 1999).

The DI threshold energy, estimated to be $(27.7 \pm 0.5) \text{ eV}$, agrees well with the SI threshold energy $(27.0 \pm 0.5 \text{ eV})$ and with the thresholds calculated by Kim *et al* (27.3 eV) and by Hitchcock *et al* (27.0 eV, 27.6 eV and 28.0 eV corresponding to the $^3\Pi$, $^1\Pi$ and $^1\Sigma^+_I$ molecular states, respectively). The weak signal observed around 25 eV may be attributed to the presence of vibrationally excited states. A similar effect is more clearly observed for DE and will be discussed in the next section.

The ionic fragmentation of CO⁺⁺ was studied by Hitchcock *et al* (1998) in a PIPICO experiment with CO in the ground state: energy thresholds were reported to form CO⁺⁺ in 11 specific states. The CO ionization potential (13.99 eV, Krishnamurthi *et al* 1991) is subtracted from these values to obtain the corresponding threshold energies from CO⁺ (table 3). According to these energies, they form three groups (table 3) containing four states for the first one (27.0–29.4 eV), five states for the second (33.0–37.1 eV) and two states for the third one (44.6–46.4 eV). The increasing slope of the DI cross section observed between 27 eV and 50 eV expresses the successive opening of the various DI channels corresponding to each of these intermediate molecular states.

Total cross sections for electron impact ionization of CO⁺ have been calculated by applying the binary-encounter-Bethe (BEB) model (Kim *et al* 2000) and the semi-classical Deutsch–Märk (DM) model (Deutsch *et al* 2003). The maximum cross sections were found to be $1.17 \times 10^{-16} \text{ cm}^2$ at 130 eV and $1.45 \times 10^{-16} \text{ cm}^2$ at 140 eV, for Kim *et al* and Deutsch *et al*, respectively.

In order to compare theoretical results with experimental data (figure 6), the total ionization cross section (σ_I) is calculated by summing present absolute DI cross sections together with SI cross sections (σ_{SI}) and ADI cross sections (σ_{ADI}) ($\sigma_I = \sigma_3 + \sigma_{\text{SI}} + \sigma_{\text{ADI}}$). The measured maximum cross section is around $1.40 \times 10^{-16} \text{ cm}^2$ at 125 eV. The DM model overestimates the DI cross section above 50 eV whereas the BEB model underestimates it. The agreement

Table 3. Threshold and KER for DE and DI.

						KER								
Processes		Threshold			Molecular state	Dissociation limit	Theoretical results		Present results					
		Present results (eV)	Other experimental results (eV)	Theoretical results (eV)			KER (eV)	Width (eV)	KER (eV)	Width (eV)				
DE	$C^+ + O + e^-$	6.1 ± 0.5	5.3 ^b	9.0 ^a	$4\Sigma^-_I$	$C^+(^2P) + O(^3P)$	0.6	0.0–1.5	1.2	0–11				
		8.5 ± 0.5	9.5 ^c	9.2 ^a	$2\Pi_{II}$		0.8	0.0–1.8						
			12.5 ^d	10.4 ^a	$2\Sigma^-_I, ^2\Delta_I, ^4\Pi_I$		2.0	0.8–3.3						
				11.5 ^a	$4\Pi_{II}$		3.1	2.2–6.5						
				12.5 ^a	$2\Sigma^-_{II}$		4.1	2.8–5.8						
				15.9 ^a	$4\Sigma^-_{II}$		7.5	6.0–9.2						
				10.4 ^a	$2\Sigma^+_{III}$	$C^+(^2P) + O(^1D)$	0.1	0.0–1.1						
				12.1 ^a	$2\Delta_{II}$		1.8	0.5–3.2						
				13.3 ^a	$2\Pi_{III}$		3.0	1.7–4.8						
				14.6 ^a	$2\Pi_{IV}, ^2\Pi_V$		4.3	3.6–5.4						
	$C + O^+ + e^-$			15.5 ^a	$2\Phi_I$		5.2	3.4–7.4	2 4	0–4 0–10				
				17.6 ^a	$2\Sigma^-_{III}, ^2\Delta_{III}$		7.3	5.9–8.7						
		12.1 ± 0.5	13.8 ^c	13.2 ^a	$6\Sigma^+_I$	$C(^3P) + O(^4S)$	2.5	0.6–4.8						
		14.8 ± 0.5		14.8 ^a	$4\Sigma^+_{II}$		4.1	2.7–5.9						
				15.6 ^a	$2\Sigma^+_{IV}$		4.9	4.1–6.4						
				16.7 ^a	$2\Pi_{VI}, ^6\Pi_I, ^4\Pi_{III}$		6.0	4.6–8.1						
		DI	$C^+ + O^+ + 2e^-$	25.1 ± 0.5	–	28.0 ^e	$1\Sigma^+_I$	$C^+(^2P) + O^+(^2D)$			2.7	0.2	7 13	2–11 2–24
				27.7 ± 0.5		27.6 ^e	1Π	$C^+(^2P) + O^+(^2D)$			2.3	0.2		
						27.0 ^e	3Π	$C^+(^2P) + O^+(^4S)$			5.0	0.2		
						29.4 ^e	$3\Sigma^-$	$C^+(^2P) + O^+(^4S)$			7.4	3.0		
				34.4 ^e	$1\Sigma^+_{II}$	$C^+(^2P) + O^+(^2P)$	7.4	1.4						
				33.0 ^e	1Δ	$C^+(^2P) + O^+(^2D)$	7.7	2.5						
				34.7 ^e	$3\Sigma^+$	$C^+(^2P) + O^+(^2D)$	9.4	0.6						
				35.9 ^e	3Δ	$C^+(^2P) + O^+(^2D)$	10.6	2.0						
				37.1 ^e	$1\Sigma^-$	$C^+(^2P) + O^+(^2D)$	11.8	1.0						
				44.6 ^e	$1\Sigma^+_{III}$	$C^+(^2P) + O^+(^2P)$	17.6	1.2						
				46.4 ^e	$1\Sigma^+_{IV}$	$C^+(^4P) + O^+(^4S)$	19.1	1.0						

^a Honjou and Sasaki (1979).^b Mitchell and Hus (1985).^c Orient and Srivastava (1987).^d Rosen *et al* (1998).^e Hitchcock *et al* (1998).

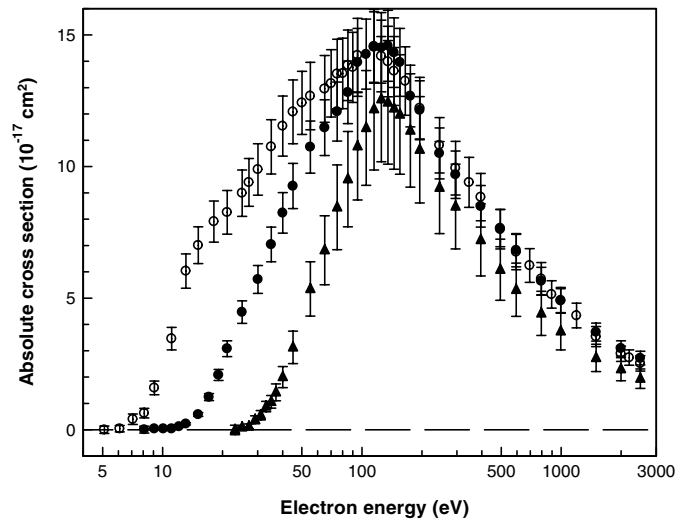


Figure 5. Absolute cross sections for the production of C^+ ($\sigma_{1.3}$ (○)) and of O^+ ($\sigma_{2.3}$ (●)); absolute cross sections for DI (σ_3 (▲)), versus electron energy.

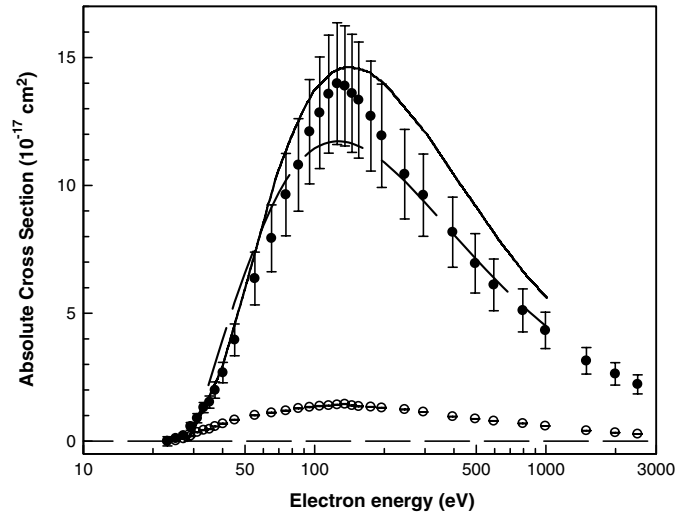


Figure 6. Total ionization cross sections (σ_I): present results (●), Deutsch *et al* (—) and Kim *et al* (---); single ionization cross section (σ_{SI}) by Belic *et al* (○).

between theory and experiment is found to be very good in the low energy region. The branching ratio in favour of DI (R_{DI}) is calculated around the maximum as follows:

$$R_{DI} = \frac{\sigma_3}{\sigma_I}. \quad (33)$$

The present result ($R_{DI} = 0.90 \pm 0.02$) confirms the dominance of dissociation following electron impact ionization of CO^+ , keeping in mind that asymmetric dissociation ionization processes are negligible. Hitchcock *et al* also analysed the relative importance of CO ionization reactions following high energy photo-absorption. At the highest photon energy available (534 eV), R_{DI} is estimated to be 0.82 which is in good agreement with the present result.

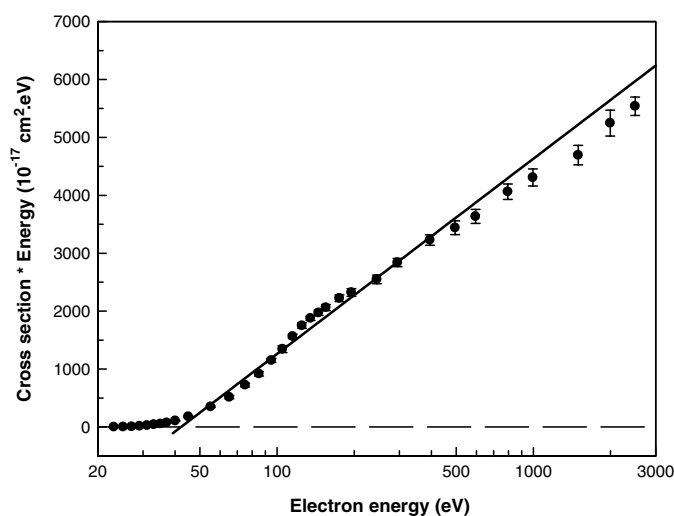


Figure 7. Bethe plot of the ionization cross section (σ_I). The full line is the result of the fit (equation (34)).

The Bethe plot of experimental data for σ_I (figure 7) shows that the data are well aligned along a straight line above 50 eV. This indicates that the energy dependence of the electron impact ionization cross section can adequately be represented by the usual Bethe form:

$$\sigma_I = \frac{a}{EI} \left[\ln \left(\frac{E}{I} \right) + b \right]. \quad (34)$$

The straight line in figure 7 is the result of the least-square fit of the cross section according to formula (34): parameters a and b are determined to be $39.5 \times 10^{-14} \text{ cm}^2 \text{ eV}^2$ and -0.45 , respectively. The Bethe energy dependence is seen to be valid well below the cross section maximum, whereas this dependence is generally supposed to be valid in the high energy range only.

3.3. Dissociative excitation cross sections

Dissociative excitation cross sections (σ_1 and σ_2) are obtained for each ion ($\sigma_1 = \sigma_{1,3} - \sigma_3$ and $\sigma_2 = \sigma_{2,3} - \sigma_3$) and results are presented in figure 8. The DE cross section values at the maximum are found to be $(9.69 \pm 2.08) \times 10^{-17} \text{ cm}^2$ for C^+ and $(6.24 \pm 1.33) \times 10^{-17} \text{ cm}^2$ for O^+ , both at about $E_e = 35 \text{ eV}$.

The threshold energies are found to be $(8.5 \pm 0.5) \text{ eV}$ and $(14.8 \pm 0.5) \text{ eV}$ for C^+ and O^+ , respectively. According to the potential energy calculations by Honjou and Sasaki (1979), the binding energy of ground state CO^+ is 8.5 eV and the C^+ formation may occur via the excitation of the lowest dissociative state ($^4\Sigma^-_1$) at about 9.0 eV, which agrees well with the present threshold. Below the observed thresholds, a small contribution is seen in both cases, which extends from (6.1 ± 0.5) to $(8.5 \pm 0.5) \text{ eV}$ for C^+ and from (12.1 ± 0.5) to $(14.8 \pm 0.5) \text{ eV}$ for O^+ . The range of this contribution ($\Delta E_e \sim 2.5 \text{ eV}$) excludes the presence of electronic excitation, as the lowest excited state ($\text{A}^2\Pi$) is located 2.57 eV above the ground state. The observed signal is most likely due to the vibrationally excited states' population where the vibrational level (v) should not exceed 10. A similar conclusion was deduced by Mitchell and Hus (1985) who measured DE cross sections in a single pass merged beam experiment: the

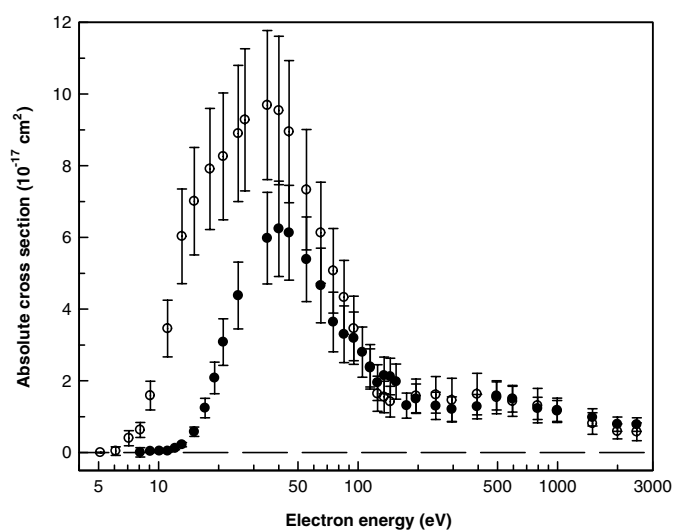


Figure 8. Absolute cross sections for dissociative excitation of CO^+ to C^+ (σ_1 (O)) and O^+ fragments (σ_2 (●)).

low observed threshold energy (5.3 eV) was attributed to the presence of electronic excitation and of vibrational excitation up to $v \sim 10$. On the other hand, the storage ring method (Rosen *et al* 1998) ensured the formation of molecular ions in the ground electronic and vibrational levels and the threshold energy was found to be higher (around 12.5 eV). Orient and Srivastava (1987) measured appearance thresholds in an electron impact ionization experiment for the CO molecule. They were found at about 23.7 eV for C^+ and 28.0 eV for O^+ , i.e. DE thresholds are 9.5 eV for C^+ and 13.8 eV for O^+ after subtraction of the CO^+ appearance threshold (14.2 eV). The subtraction is justified because the equilibrium internuclear distances are almost identical for CO and for CO^+ , so that the respective Franck–Condon regions overlap. The agreement between the different results (see table 3) is reasonable keeping in mind very different experimental approaches and target conditions in the experiments.

Calculated DE energy thresholds extend from 9.0 to 17.6 eV and, as observed for DI, the increasing slope of the present cross section between 8.5 eV and 18 eV reflects the successive opening of all the DE channels. Due to the absence of vibrationally excited states and according to the observed threshold (12.5 eV), Rosen *et al* restricted the possible transitions to the $^2\Pi_{\text{III}}$, $^2\Pi_{\text{IV}}$ and $^2\Pi_{\text{V}}$ states, leading to dissociation limit where oxygen atoms are formed in the first excited state (^1D). In contrast, the present experiment indicates that ground state (^3P) oxygen atoms are also formed.

The threshold observed for O^+ production (14.8 ± 0.5 eV) shows that the lowest state ($^6\Sigma^+_{\text{I}}$) is weakly populated, so that DE probably proceeds via the $^4\Sigma^+_{\text{II}}$ state (14.8 eV) and other excited states.

Around the maximum (40 eV) σ_1 is about 50% larger than σ_2 , but in the high energy range (above 100 eV) both cross sections are found to coincide. In order to compare present results with previous ones (Mitchell and Hus 1985, Rosen *et al* 1998) σ_1 and σ_2 are summed. Present data (figure 9) are found to be lower than others by some 30% in the region of the maximum, though error bars are not fully disconnected from each other. In the Mitchell's experiment, the vibrational population is similar to the present one, but electronic excitation of CO^+ ions is also possible (see above), which could probably explain the presently observed discrepancy.

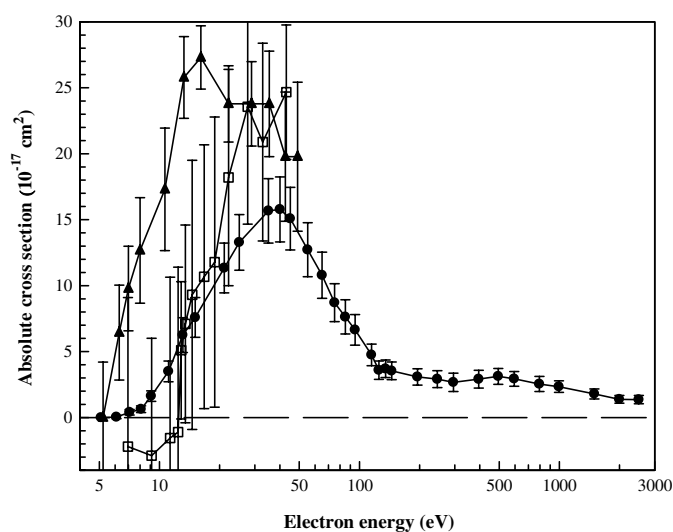


Figure 9. Total DE cross sections ($\sigma_1 + \sigma_2$): present results (\bullet), Mitchell *et al* (\blacktriangle) and Rosen *et al* (\square).

A significant vibrational population strongly increases the signal around the threshold, as it was dramatically observed for H_2^+ (Abdellahi *et al* 2004). Internal excitation being estimated to be totally absent in the Rosen's experiment, one should expect corresponding cross sections to be slightly lower than the two other sets of results, but no argument could be invoked to explain the present situation.

3.4. KER distributions for C^+ and O^+

Kinetic energy release distributions are obtained for C^+ and O^+ (figures 10 and 11, respectively), at electron energies of 17.1, 25.1, 45.1, 145.1 and 495.1 eV where magnetic scans were performed.

At the lowest incident electron energy (17.1 eV, below the DI threshold), the C^+ distribution, due to DE only, mainly consists of a narrow peak centred on 1.2 eV. On the high energy side of this peak, a weak contribution appears which cannot be isolated. The comparison with calculated data indicates that the peak is due to the $^4\Sigma^-_1$, $^2\Pi_{II}$ and $^2\Sigma^+_{III}$ states which exhibit very low KER and to the $^2\Sigma^-_1$, $^2\Delta_1$, $^4\Pi_1$, $^2\Delta_{II}$ states with KER around 2 eV. The shoulder illustrates the role of the other states whose KER extend from 3.0 eV to 7.5 eV. At higher electron energies, the DE peak is seen to decrease substantially and two DI contributions appear in the KER ranges 2–11 eV and 11–24 eV. These peaks clearly dominate the distribution at 145.1 eV and 495.1 eV. This confirms the reduced role of DE with respect to DI as deduced from the above discussions.

For O^+ , as expected, the DE peak is very weak at 17.1 eV. The low KER range looks almost empty, as, by comparison with calculated data, no state can induce KER around zero. The lowest state ($^6\Sigma^+_1$) is probably faintly populated and should contribute to KER around 2 eV only. At 25.1 eV, contributions of other states ($^4\Sigma^+_{II}$ and above) are observed for KER below 10 eV. At high energies, the DI peaks are also well observed. For comparison, KERDs at 495.1 eV are displayed for C^+ and for O^+ (figure 12). These two distributions are seen to be very similar, which is easily understood because both ions are formed in the same DI

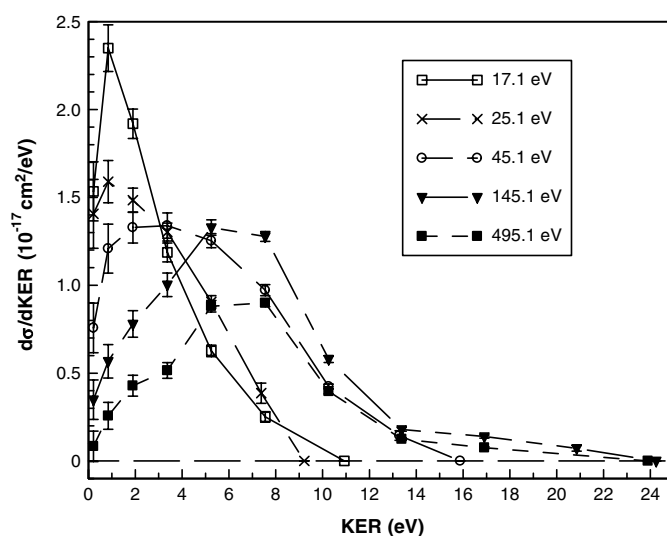


Figure 10. Kinetic energy release distributions of C^+ fragments for indicated electron energies.

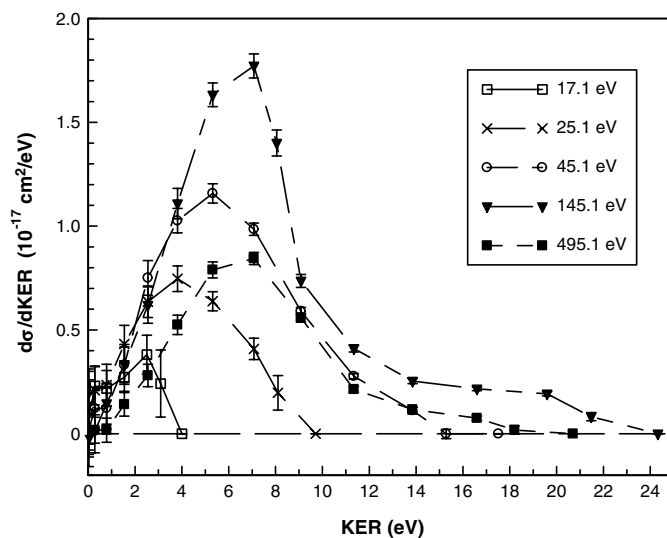


Figure 11. Kinetic energy release distributions of O^+ fragments for indicated electron energies.

reaction (3). For the C^+ fragment, the small DE contribution can still be noted for KER lower than 4 eV.

KERDs have been tentatively decomposed into their partial contributions by fitting the data with Gaussian functions for the two DI peaks. For DE, we adopted the function (not a Gaussian shape) fitting the KERD at 17.1 eV. The three contributions are well isolated both for C^+ and for O^+ at 145.1 eV (figures 13 and 14, respectively). The DI peaks are centred around 7 eV and 13 eV, respectively. The first one, extending from 2 to 11 eV, seems to be mainly due to the group of states ($^3\Sigma^-$, $^1\Sigma^+_{II}$ and $^1\Delta$) centred on 7.5 eV. The second one is seen to be very broad (2–24 eV), the four highest states ($^3\Delta$, $^1\Sigma^-$, $^1\Sigma^+_{III}$ and $^1\Sigma^+_{IV}$) are probably responsible for the high KER tail of the distribution.

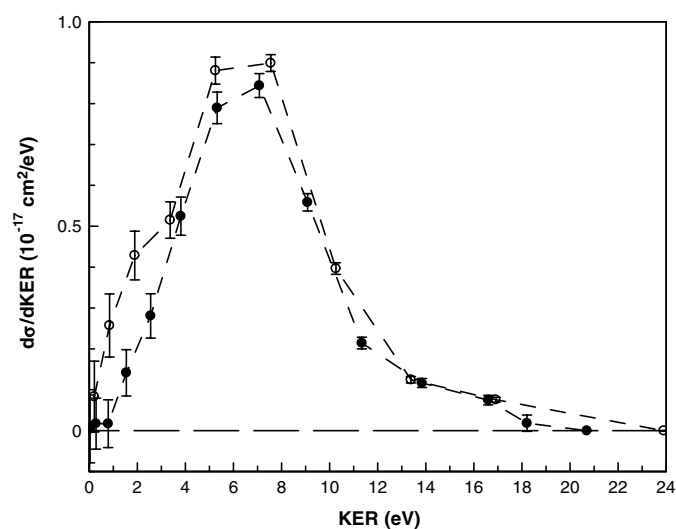


Figure 12. KERDs for C^+ (\circ) and for O^+ (\bullet) fragments at 495.1 eV.

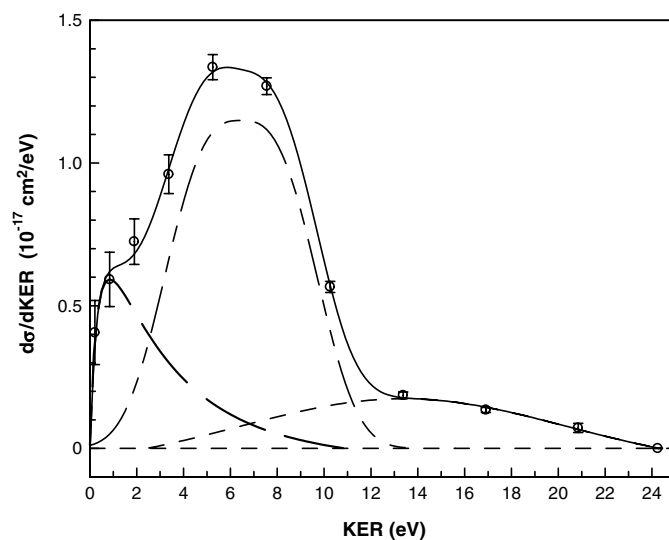


Figure 13. Contributions of DE (—) and of DI (---, first group and ---, second group) to the C^+ KERD at 145.1 eV. For details, see the text.

3.5. Angular anisotropy of dissociation fragments

The anisotropy factor ε is determined at electron energies where magnetic scans were performed. Results are presented in figure 15 together with the associated total uncertainties (90% confidence limit). The small values ($\varepsilon \leq 0.06$) obtained over the whole energy range for both C^+ and O^+ indicate that the angular fragment distribution differs weakly from the isotropic one. According to the preceding discussions, the low values obtained at 17.1 eV correspond to DE and the constant value, which is reached at high energy, corresponds to DI.

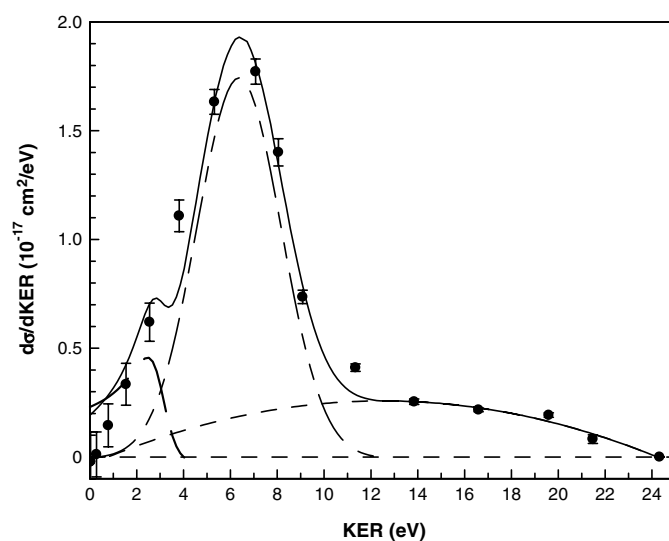


Figure 14. Contributions of DE (—) and of DI (---, first group and - - -, second group) to the O^+ KERD at 145.1 eV. For details, see the text.

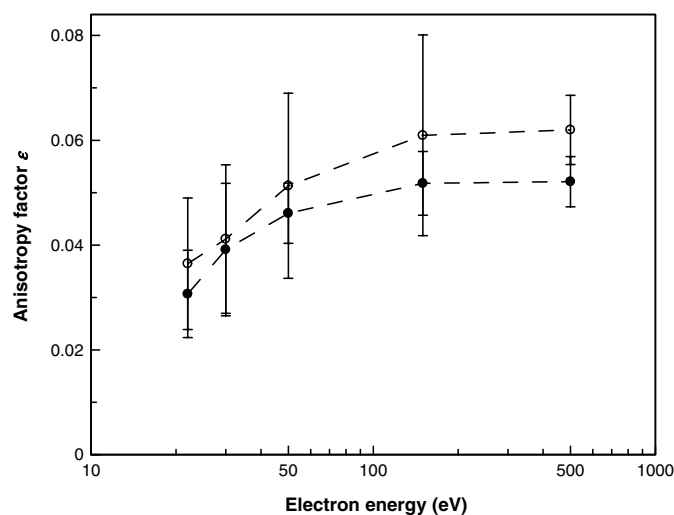


Figure 15. Anisotropy factor (ϵ) versus electron energy for C^+ (O) and for O^+ (●) fragments.

4. Summary

First absolute cross sections for electron impact dissociative excitation and ionization of CO^+ to C^+ and O^+ fragments are reported in the energy range from threshold to 2.5 keV. Both the experimental set-up and the data analysis procedures are described in details for the estimation of (i) the absolute cross sections, (ii) the kinetic energy release distributions and (iii) the anisotropies. The DE and DI contributions are separated from each other by analysing the shape of the cross section. For ionization, the results show that the DI cross section largely exceeds the SI one, confirming that CO^{++} dissociates rapidly. Good agreements are found

between experimental results and predictions of theoretical models for the ionization cross section (Kim *et al* 2000, Deutsch *et al* 2003). For DE, the apparent disagreement between present results and those of Mitchell and Hus (1985) and of Rosen *et al* (1998) is probably due to differences in the respective excited (electronic and vibrational) populations. The role of the group of states contributing to the different processes is discussed by comparing the present energies' thresholds values and the KERDs with theoretical values for DE (Honjou and Sasaki 1979) and for DI (Hitchcock *et al* 1998). The angular distributions are found to be weakly dependent on the molecule orientation, as the anisotropy lies in the range 0.03–0.06 over the whole energy range.

Acknowledgments

The authors acknowledge the financial support of the Association Euratom-Belgian State and the technical support of C Alaime and D Dedouaire. They are indebted to the Forschungszentrum Jülich for lending the ECR ion source.

References

- Abdellahi E I, Ghazaly M O, Jureta J, Urbain X and Defrance P 2004 *J. Phys. B: At. Mol. Opt. Phys.* **37** 2467
- Bahati E M, Jureta J J, Belic D S, Cherkani-Hassani H, Abdellahi M O and Defrance P 2001a *J. Phys. B: At. Mol. Opt. Phys.* **34** 2963
- Bahati E M, Jureta J J, Belic D S, Rachafi S and Defrance P 2001b *J. Phys. B: At. Mol. Opt. Phys.* **34** 1757
- Belic D S, Yu D J, Siari A and Defrance P 1997 *J. Phys. B: At. Mol. Opt. Phys.* **30** 5535
- Bodeldijk M 1996 *Thesis* Institute for Atomic and Molecular Physics (AMOLF), Amsterdam
- Bodeldijk M, Van der Zande W and Kistemaker P G 1994 *Chem. Phys.* **179** 125
- Busalla A, Blum K, Beyer T and Nestmann B M 1999 *J. Phys. B: At. Mol. Opt. Phys.* **32** 791
- Defrance P, Brouillard F, Claeys W and Van Wassenhove G 1981 *J. Phys. B: At. Mol. Phys.* **14** 103
- Deutsch H, Becker K, Defrance P, Onthong U, Probst M, Matt S, Scheier P and Märk T D 2003 *Int. J. Mass Spectrom.* **223–4** 639
- Djuric N, Chung Y S, Wallbank B and Dunn G H 1997 *Phys. Rev. A* **56** 2887
- Erickson N R, Snell R L, Loren R B, Mundy L and Plambeck R L 1981 *Appl. J.* **245** L83
- Harrison M F A 1968 *Methods in Experimental Physics* vol 7B ed W L Fite and B Bederson p 95
- Heubner W F and Giguere P T 1980 *Appl. J.* **238** 753
- Hitchcock A P, Lablanquie P, Morin P, Lizon E, Lugrin A, Simon M, Thiry P and Nenner I 1998 *Phys. Rev. A* **37** 2448
- Honjou N and Sasaki F 1979 *Mol. Phys.* **37** 1593
- Kim Y K, Irikura K K and Ali M A 2000 *J. Res. Natl. Stand. Technol.* **105** 285
- Khouilid M, Cherkani-Hassani S, Rachafi S, Teng H and Defrance P 2001 *J. Phys. B: At. Mol. Opt. Phys.* **34** 1727
- Krishnamurthi V, Nagesha K, Marathe V R and Mathur D 1991 *Phys. Rev. A* **44** 5460
- Mitchell J B A and Hus H 1985 *J. Phys. B: At. Mol. Phys.* **18** 547
- Orient O J and Srivastava S K 1987 *J. Phys. B: At. Mol. Phys.* **20** 3923
- Rosen S, Peverall R, Larsson M, Le Padellec A, Semaniak J, Larson A, Stromholm C, Van der Zande, Danared H and Dunn G H 1998 *Phys. Rev. A* **57** 4462
- Siari A, Belic D S, Defrance P and Rachafi S 1999 *J. Phys. B: At. Mol. Opt. Phys.* **32** 587
- Störzer H, Stutzki J and Sternberg A 1995 *Astron. Astrophys.* **296** L9
- Zare R N 1967 *J. Chem. Phys.* **47** 204